Journal of Materials Chemistry A

PAPER

View Article Online
View Journal | View Issue

Cite this: J. Mater. Chem. A, 2019, 7, 4119

In situ formation of highly controllable and stable Na_3PS_4 as a protective layer for Na metal anode†

Yang Zhao, ‡[a] Jianwen Liang,‡[a] Qian Sun,[a] Lyudmila V. Goncharova,[b] Jiwei Wang,[a] Changhong Wang,[a] Keegan R. Adair,[a] Xiaona Li,[a] Feipeng Zhao,[a] Yipeng Sun,[a] Ruying Li[a] and Xueliang Sun *[a]

Received 23rd October 2018
Accepted 21st January 2019

DOI: 10.1039/c8ta10174d

rsc.li/materials-a

Na metal is considered as a promising anode material for Na metal batteries (NMBs) due to its high theoretical specific capacity and low electrochemical potential. However, the Na metal anode faces several challenges, including: (1) safety concerns related to dendrite formation; (2) low coulombic efficiency (CE) and poor cycling performance caused by the unstable solid electrolyte interphase (SEI); (3) an infinite volume change due to its hostless nature. In this paper, we demonstrate for the first time a facile and *in situ* solution-based method to synthesize an artificial protective layer of Na_3PS_4 (NaPS) on the surface of Na metal. Promisingly, the thickness and composition of the NaPS can be controlled through adjustment of the precursor concentration and reaction times. The thin amorphous NaPS layers on the surface of the Na metal will reduce parasitic side reactions with electrolyte components, increase the homogeneity of the SEI layer and improve the Na^+ flux on the surface. Meanwhile, the ionically conductive NaPS can eliminate the strong electric field buildup at the surface, resulting in a more homogeneous Na plating/stripping process with suppressed Na dendrite growth. The design of the NaPS-coated Na anode opens up new opportunities for the realization of next-generation high-energy density Na metal batteries.

Introduction

Na-ion batteries (NIBs) and Na metal batteries (NMBs) are considered as promising alternatives to the conventional Li-ion batteries for large-scale energy storage applications due to the wide availability and low cost of sodium sources.[1] In addition, NMBs, including room temperature Na–S and Na–air batteries, show high theoretical specific energy densities of 1274 W h kg^{-1} and 1605 W h kg^{-1}, respectively.[2,3] Metallic Na is the ultimate choice among all the possible anode candidates due to its high theoretical capacity and low electrochemical potential.[4] However, metallic Na suffers from several challenges during electrochemical cycling, including: (1) the high reactivity between Na and the liquid electrolyte causes the formation of a solid electrolyte interphase (SEI) on the surface of Na metal. The unstable SEI layers lead to continuous consumption of the liquid electrolyte and shortening of the cycling lifetime.[5] (2) The inhomogeneous ionic flux on the surface of Na will result in mossy or dendritic Na growth, which can further lead to the formation of "dead Na", lower the coulombic efficiency (CE) and cause safety concerns due to the risk of dendrite growth and short-circuiting.[6] (3) The hostless nature of the Na metal anode results in large volume changes during repetitive Na plating/stripping processes.[7–9]

To date, different approaches have been proposed to address the aforementioned challenges of metallic Na, including electrolyte modification, the design of 3D hosts and current collectors, and surface coating/modification.[10–21,31–33] In previous studies, it has been demonstrated that using ultra-concentrated electrolytes or additives such as fluoroethylene carbonate (FEC) can stabilize the SEI layer and reduce dendrite growth.[22,23] Alternatively, surface coating/modification is another effective strategy to achieve stable artificial SEI layers which can suppress Na dendrite growth and increase the lifetime of NMBs.[24–26] In our previous studies, we demonstrated inorganic Al_2O_3 and organic–inorganic hybrid alucone (Al–ethylene glycol) thin films as protective layers for Na metal anodes, achieving enhanced electrochemical stability and cycling life in ether-based and carbonate-based electrolytes, respectively.[27,28] In order to achieve ideal artificial SEI layers, a high ionic conductivity coating which can lead to the uniform distribution of ion flux and localized current densities should be developed. Recently, Nazar's group described an efficient way to stabilize Li plating using the Li^+ ion solid electrolyte Li_3PS_4 as a surface modification for Li metal anodes.[29] The Li_3PS_4 layer

[a]Department of Mechanical and Materials Engineering, University of Western Ontario, London, Ontario, N6A 5B9, Canada. E-mail: xsun@eng.uwo.ca

[b]Department of Physics and Astronomy, University of Western Ontario, London, Ontario, N6A 3K7, Canada

† Electronic supplementary information (ESI) available. See DOI: 10.1039/c8ta10174d

‡ These authors contributed equally to this work.

was chemically and electrochemically stable over repeated plating/stripping cycles and delivered more stable plating/stripping performances compared to the control Li foil. To the best of our knowledge, there are still no reports on use of Na^+ ion conductive solid-state electrolytes (SSEs) as an artificial protective layer to address the instability and dendrite growth of the Na metal anode.

Herein, we demonstrate a facile and *in situ* solution-based approach to fabricate an SSE protective layer of Na_3PS_4 (NaPS) on the surface of Na metal. Promisingly, the thickness and composition of the NaPS can be controlled through the adjustment of the concentrations of precursors and reaction times. The thin amorphous NaPS layers on the Na (Na@NaPS) will reduce the reactions with the electrolytes and increase homogeneity of the SEI layers and Na^+ flux. Meanwhile, the NaPS protective layer on the surface of Na metal can facilitate homogeneous Na plating/stripping processes, leading to the suppressed Na dendrite growth. Our design of the SSE NaPS-coated Na anode opens up new opportunities for the realization of next-generation high energy density Na metal batteries.

Results and discussion

The SSE NaPS protective layers are formed by a simple *in situ* solution-based method. As shown in Fig. 1(a), sulfur-rich phosphorus sulfide molecules (P_4S_{16}) are used as precursors to react with Na metal directly in a diethylene glycol dimethyl ether (DEGDME) solvent. The reaction between Na metal and P_4S_{16} is shown as:

$$12Na + P_4S_{16} = 4Na_3PS_4$$

Due to the high reactivity between Na metal and P_4S_{16}, the reactions are expected to be controlled with different precursor concentrations and reaction times. The experimental design parameters are shown in Table S1.† First, the concentrations of the P_4S_{16} precursor in DEGDME are controlled at 0.5 mg mL^{-1}, 1 mg mL^{-1}, and 1.5 mg mL^{-1} and used with a constant reaction time of 15 min. The samples in this experiment are named Na@NaPS-1, Na@NaPS-2 and Na@NaPS-3, respectively. Second, the samples with a constant concentration of 1.5 mg mL^{-1} are used to study the effect of longer reaction times (60 min and 90 min), and these samples are named Na@NaPS-4 and Na@NaPS-5, respectively.

Rutherford backscattering spectrometry (RBS) measurements were performed on Na@NaPS-1 to Na@NaPS-5 to confirm the film thicknesses on the Na and deduce the elemental depth profiles. Fig. 1(b) shows the RBS spectrum and simulated depth profiles for Na@NaPS-3. The presence of P and S peaks from the surface can confirm the successful synthesis of the NaPS films on the Na foil. Fig. S1† shows the RBS spectra and simulated depth profiles for another samples of Na@NaPS-1 (a), Na@NaPS-2 (b), Na@NaPS-4 (c), and Na@NaPS-5 (d). Notably, by increasing the concentration of P_4S_{16} in DEGDME, the thickness of the NaPS coating increases from 120 nm to 220 nm, as shown in Fig. 1(c). Meanwhile, the content of both P and S increases as well (Table S2†). When keeping the concentration of P_4S_{16} constant at 1.5 mg mL^{-1}, the RBS results indicate that the ratio of Na to P and S stays constant and the thicknesses increase to 300 and 380 nm for Na@NaPS-4 and Na@NaPS-5 with increasing reaction times (Fig. 1(c) and Table S2†). Thus, it can be concluded from the RBS results that the thickness and composition of the NaPS films can be controlled by adjusting the concentration of P_4S_{16} and reaction times.

To further confirm the chemical compositions of the NaPS films, X-ray photoelectron spectroscopy (XPS) was performed for typical samples of P_4S_{16}, Na@NaPS-1, Na@NaPS-3 and Na@NaPS-5. Fig. S3(a) and (b)† show the high-resolution XPS spectrum of S 2p and P 2p for the P_4S_{16}, respectively. The peaks of S $2p_{1/2}$ and $2p_{3/2}$ at 164.8 eV and 163.6 eV correspond to the P–S–P bonding in P_4S_{16}. Meanwhile, the peaks of P $2p_{1/2}$ and $2p_{3/2}$ at 135.2 eV and 134.4 eV can be assigned to the P–S in P_4S_{16}. Fig. 1(d) and S2† present the XPS survey spectra of Na@NaPS-1, Na@NaPS-3 and Na@NaPS-5, where the S and P peaks can be obviously observed, consistent with the RBS results. From the high-resolution P 2p spectra for Na@NaPS-3, several peaks in the high-resolution P 2p spectra can be fitted with different distinct doublets. The double peaks of P $2p_{1/2}$ and $2p_{3/2}$ at 133.8 eV and 133.0 eV can be assigned to phosphorous in PS_4^{3-}.[29] Meanwhile, the peaks at 133.0 eV and 132.21 eV are related to the bond of P–S in $P_2S_7^{4-}$.[30,31] The XPS results indicate that the content of PS_4^{3-} and $P_2S_7^{4-}$ is 56% and 44% for NaPS-3, respectively. In the S 2p spectra, the S $2p_{1/2}$ and $2p_{3/2}$ peaks at 162.5 eV and 161.6 eV are attributed to the P=S bond in the PS_4^{3-} species. Very interestingly, from the high-resolution P 2p spectra for Na@NaPS-1 (Fig. S3(d)†), not only the PS_4^{3-} peak can be observed, but also the un-reacted P_4S_{16} peak exists, indicating the incomplete reaction between Na and P_4S_{16} with a low concentration of the precursor and a shorter reaction time. However, the P 2p spectra for Na@NaPS-5 are almost the same as those for Na@NaPS-3, indicating that the final coating layer is a mixture of both Na_3PS_4 and $Na_4P_2S_7$. All the XPS results indicate that the Na_3PS_4 films are successfully synthesized on the surface of Na foil through the *in situ* solution-based method.

Time-of-flight secondary ion mass spectrometry (TOF-SIMS) was performed to further probe the compositions of the NaPS film and element depth distributions. Fig. 2(a) shows the secondary ion images of Na^-, P^-, S^-, S_2^- and S_3^- with the magnified images on the edges after sputtering. Because of the sample exposure to air during the transferring process, the surfaces of the samples are oxidized and no species related to Na_3PS_4 films can be observed at the initial stage of analysis. However, after sputtering by Cs^+ ions, the different negative ions of P^-, S^-, S_2^- and S_3^- are visible from the edge of the sputtering areas, which are attributed to the Na_3PS_4 film on Na foil. Fig. 2(b) presents the cross-sectional ion images of S^- species for Na@NaPS-3, indicating the formation of a continuous Na_3PS_4 film from the surface down to the bulk Na. Fig. S4† displays similar ion images of Na^-, P^-, S^-, S_2^- and S_3^- for Na@NaPS-1 and Na@NaPS-5, demonstrating that the same Na_3PS_4 film was formed under different experimental conditions. The TOF-SIMS depth profiles of Na^-, P^-, S^-, S_2^- and S_3^- for Na@NaPS-3 are shown in Fig. 2(c). As expected, the signals

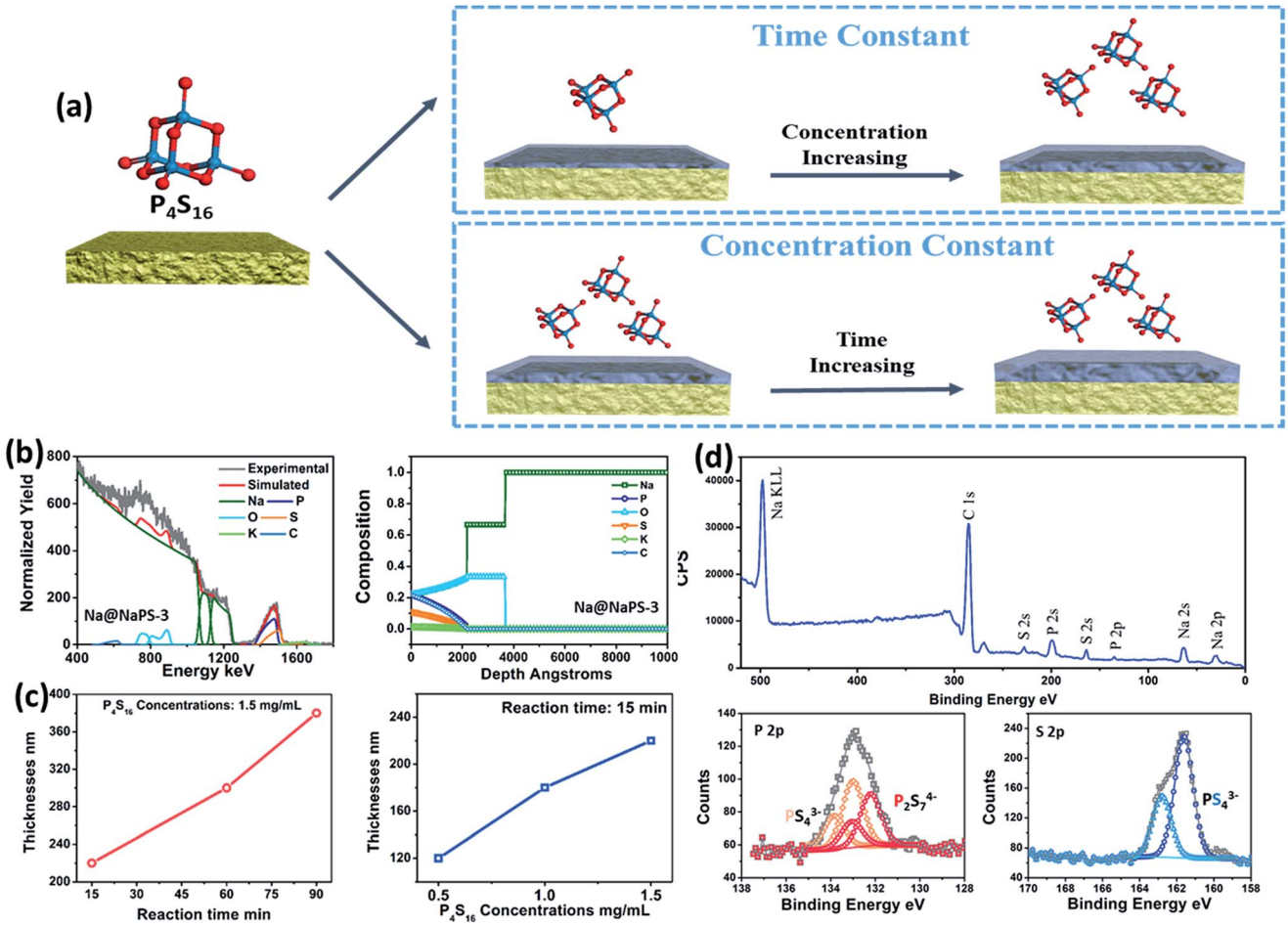

Fig. 1 (a) Schematic diagram of the *in situ* fabrication process of NaPS on Na foil; (b) RBS spectra and calculated depth profiles of Na@NaPS-3; (c) the thicknesses of different samples related to precursor concentrations and reaction times; (d) XPS survey spectra and P 2p and S 2p high-resolution spectra for Na@NaPS-3.

of P^-, S^-, S_2^- and S_3^- decrease whereas the signal of Na^- remains constant after 800 s Cs^+ sputtering. The TOF-SIMS analysis demonstrates that Na (or Na^+) species exists from the surface of the Na_3PS_4 coating layer down to the bulk Na metal. Fig. S5† shows the depth profiles of Na@NaPS-1 and Na@NaPS-5, where it can be observed that bulk Na can be reached after sputtering times of 200 s and 1300 s, respectively. The TOF-SIMS analysis further confirms that with increasing the concentration of P_4S_{16} and reaction times, the NaPS films grow thicker.

Through a combination of characterization techniques such as RBS, XPS and TOF-SIMS, it can be concluded that Na_3PS_4 films with controlled thicknesses have been successfully synthesized on Na foils by the *in situ* solution-based method. Moreover, from the XRD patterns shown in Fig. S6,† the as-prepared Na_3PS_4 are amorphous without any characteristic XRD signatures. The three main peaks in the XRD patterns are attributed to the cubic Na metal.[15] The morphologies of Na@NaPS-1, Na@NaPS-3 and Na@NaPS-5 are presented in Fig. S7 and S8.† From the top view SEM images shown in Fig. S7(a–d),† smooth and continuous films are formed on the surface of both Na@NaPS-1 and Na@NaPS-3. However, a rougher surface with larger particle sizes is obtained with a longer reaction time and higher precursor concentration for Na@NaPS-5 (Fig. S7(e and f)†). From the cross-sectional SEM images (Fig. S8†), it can be observed that the NaPS layer grows thicker from Na@NaPS-1 to Na@NaPS-5. In brief, the trend of the thickness as a function of the concentration of the P_4S_{16} solution and the reaction time are well consistent with the RBS, TOF-SIMS, and SEM results.

Galvanostatic cycling of the Na_3PS_4 coated Na and bare Na foil was performed using the symmetrical cell configuration of Na@NaPS/separator/Na@NaPS, using 1 M $NaPF_6$ electrolyte dissolved in 1 : 1 (v/v) EC : PC. Fig. 3(a) presents a comparison of the cycling stability of Na@NaPS-3 and bare Na foil at a current density of 1 mA cm^{-2} with a capacity of 1 mA h cm^{-2}. The thickness effects of NaPS on the electrochemical performances will be discussed in the following part. For pristine Na foil, the initial stripping/plating over-potential is about 200 mV (*versus* Na^+/Na). Subsequently, the over-potential starts to increase after 150 h and reaches 4000 mV after 160 h. It can be observed that the pristine Na foil suffers from unstable voltage profile fluctuations, resulting in short circuiting of the cell. Promisingly, the Na@NaPS-3 delivers a slightly larger over-potential in the first plating process and then stabilizes in the

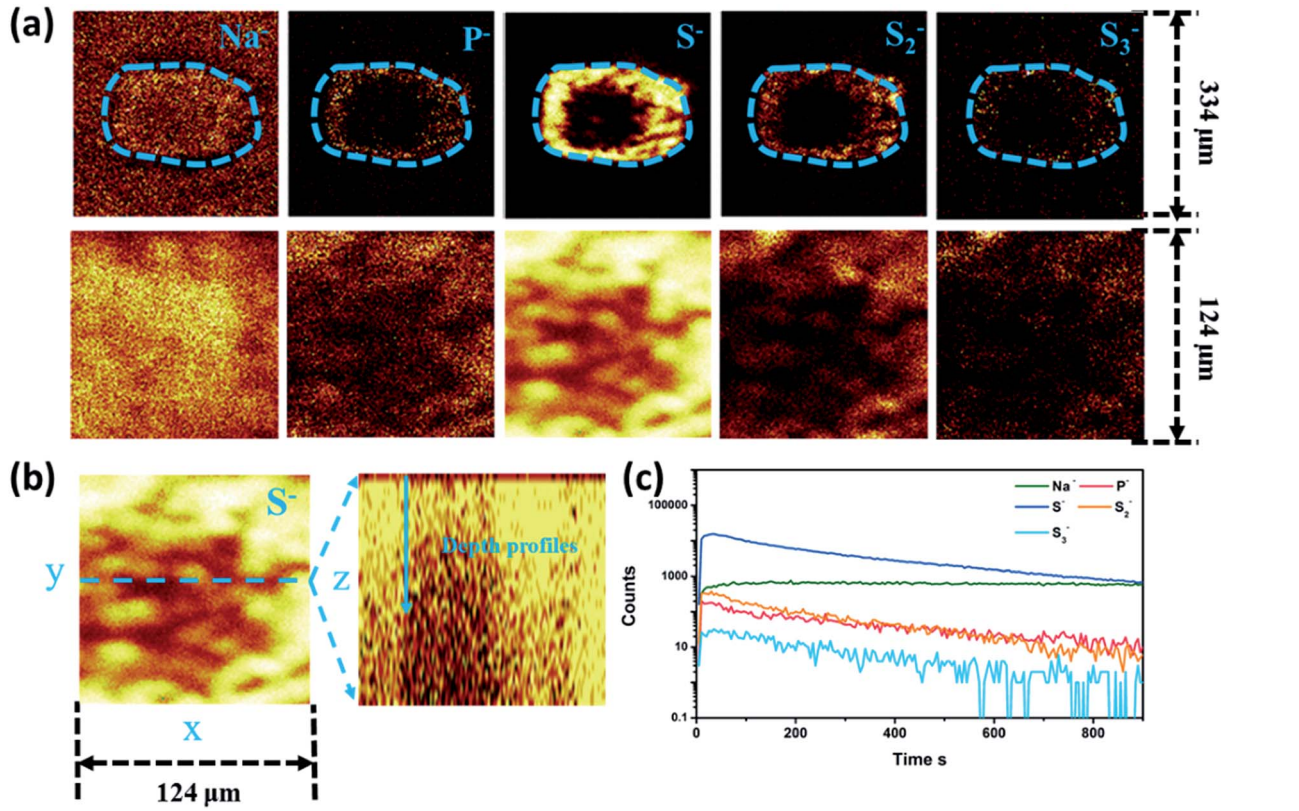

Fig. 2 (a) TOF-SIMS chemical ion images of the Na^-, P^-, S^-, S_2^-, and S_3^- species for Na@NaPS-3 (Blue circle: sputtering areas); the analysis area was 300 × 300 μm^2 and the sputtering area was 100 × 100 μm^2. (b) Cross-sectional ion images of S^- species for Na@NaPS-3; (c) TOF-SIMS depth profiles of Na^-, P^-, S^-, S_2^-, and S_3^- species for Na@NaPS-3.

following cycles with an over-potential of 300 mV (*versus* Na^+/Na), which can be sustained for more than 270 h. The potential profiles of Na@NaPS-3 and bare Na foil are also shown in Fig. 3(a), in which the Na foil displays unstable over-potentials with large polarization and Na@NaPS-3 presents smoother profiles with a negligible increase in hysteresis. On increasing the current density to 3 mA cm^{-2}, the over-potential of pristine Na is seen to rapidly increase after only 70 h (Fig. 3(b)). Furthermore, the over-potential reaches over 5000 mV (*versus* Na^+/Na) after 115 h, which is the voltage cut-off limitation in the testing. Promisingly, the Na@NaPS-3 maintains improved stability at a higher current density with a lower over-potential of 500 mV after 140 h. In the previously reported literature, the cycling capacity of metal anodes (for both Li and Na metal anodes) in symmetrical cell testing is usually around 1 mA h cm^{-2} or even lower, which cannot meet the requirements for practical applications. Herein, we also demonstrate the Na@NaPS-3 with a large capacity of 3 mA h cm^{-2} compared with bare Na foil under the same testing conditions. Fig. 3(c) presents the cycling stability and voltage profiles of both Na@NaPS-3 and bare Na foil using a high capacity limit of 3 mA h cm^{-2} at a current density of 1 mA cm^{-2}. The bare Na foil exhibits an unstable plating/stripping behavior after 100 h of cycling with increasing over-potentials which rise to 3000 mV after 180 h (Fig. 3(c)). However, the Na@NaPS-3 displays a stable cycling performance with an over-potential of only 300 mV after 250 h, which is almost 10 times lower than what was observed for bare Na foil. Based on these observations, it can be concluded that the NaPS coating is an excellent protective layer for the Na metal anode in applications that require a large capacity.

To understand the relationship between thickness, composition and electrochemical performance, the other samples of Na@NaPS-1, Na@NaPS-2, Na@NaPS-4, and Na@NaPS-5 were studied at a current density of 1 mA cm^{-2} with cycling capacities of 1 mA h cm^{-2} and 3 mA h cm^{-2}. Fig. S9† shows the electrochemical performances of samples obtained with lower P_4S_{16} concentrations for Na@NaPS-1 and Na@NaPS-2. From the results, it can be seen that both Na@NaPS-1 and Na@NaPS-2 exhibit better performances than the bare Na foil, in which the stability of Na@NaPS-2 appears to be enhanced compared to that of Na@NaPS-1. However, they are still not comparable to Na@NaPS-3. From the above discussion, it can be seen that the NaPS coating becomes thicker with an increase in the P_4S_{16} concentration. Furthermore, we find that the thicknesses of the NaPS protective layers have a significant influence on the electrochemical performances. The higher P_4S_{16} concentrations leading to thicker coatings (Na@NaPS-3) show the best benefits in terms of plating/stripping performances. Furthermore, the cycling stabilities of the samples of Na@NaPS-4, Na@NaPS-5 with longer reactions are presented in Fig. S10.† The performances of Na@NaPS-4 and Na@NaPS-5, appear to be inferior to

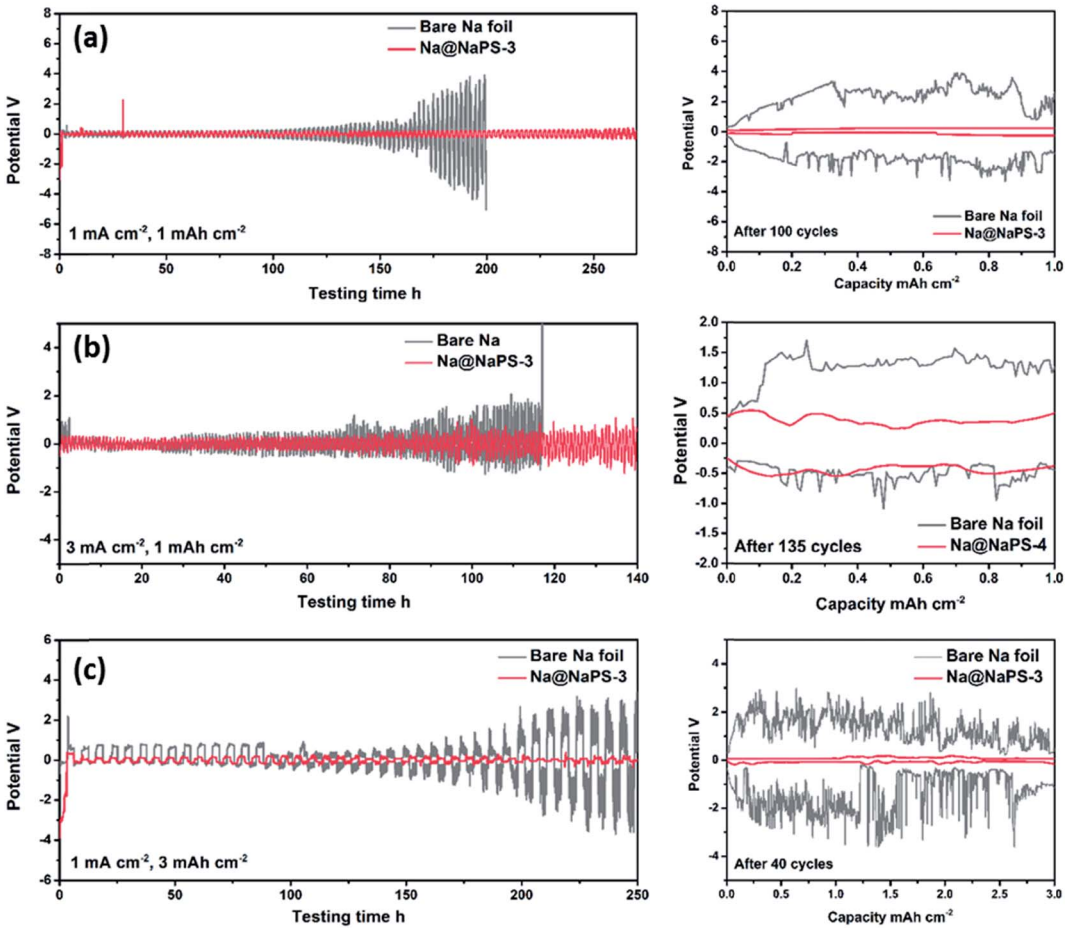

Fig. 3 (a) Comparison of the cycling stability and potential profiles of the Na@NaPS-3 and bare Na foil at a current density of 1 mA cm^{-2} with a capacity of 1 mA h cm^{-2}; (b) the cycling stability and potential profiles of the Na@NaPS-3 and bare Na foil at a current density of 3 mA cm^{-2} with a capacity of 1 mA h cm^{-2}; (c) the cycling stability and potential profiles of the Na@NaPS-3 and bare Na foil at a current density of 1 mA cm^{-2} with a capacity of 3 mA h cm^{-2}.

that of the bare Na foil. The reasons could be explained as follows: (1) From Fig. S7,† a rougher surface with larger particle sizes is obtained with a longer reaction time and a higher precursor concentration for Na@NaPS-5. The rougher surface with large particles could lead to the nonuniform distribution of the Na^+ flux during electrochemical cycling, which will aggravate the mossy-like and dendritic Na growth. (2) From the cross-sectional view SEM images (Fig. S8†), it can be observed that NaPS-5 with a longer reaction time presents a porous structure of the coating layer compared to NaPS-3. This porous structure of the coating layer could still cause side reactions between the Na metal and liquid electrolyte, leading to even worse performances. This result indicates that the coating thickness (from RBS and SIMS results) and surface roughness (from SEM results) are critical parameters and excessive coating can lead to poor electrochemical performances. Thus, the Na@NaPS-3 with a Na_3PS_4 layer of ~220 nm displays the best electrochemical performances with respect to cycling current density and capacity.

The performance of the bare Na foil and Na@NaPS-3 as anodes for NMBs was further investigated in a full cell using a $NaCrO_2$/C cathode. The loading of $NaCrO_2$/C is ~8 mg cm^{-2} corresponding to an areal capacity of ~1.1 mA h cm^{-2}. Fig. S11† presents the cycling performances of full cells using bare Na foil and Na@NaPS-3 as the anode at a rate of 1C (~1.1 mA cm^{-2}). In the batteries using bare Na foil, the specific capacity drops to 35 mA h g^{-1} after 75 cycles due to the poor cyclability of the planar Na foil. Promisingly, the Na@NaPS-3 anode can enable full cells that can maintain a stable capacity of 106 mA h g^{-1} over 75 cycles. The cycling stability and capacity retention demonstrate that the NaPS protective layer can effectively improve the electrochemical performances compared to the Na foil in a full cell format.

In order to understand the enhanced performance of the NaPS-coated Na anode compared to that of the pristine Na foil, the morphologies of Na@NaPS-3 and Na foil after cycling were analyzed by SEM. Fig. 4(a and b) compare the SEM images of Na@NaPS-3 and Na foil after 10 cycles of electrochemical plating/stripping at a current density of 1 mA cm^{-2} with a capacity limit of 1 mA h cm^{-2}. From the SEM images shown in Fig. 4(a), Na dendrites with moss-like structures of approximately 10–20 μm can be clearly observed for bare Na foil after

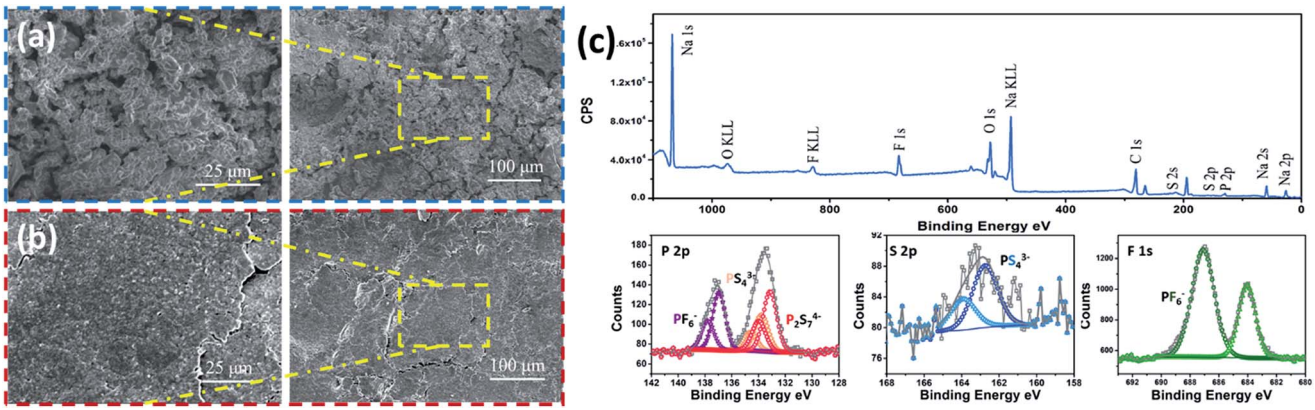

Fig. 4 Top-view SEM images of the bare Na foil (a) and Na@NaPS-3 (b) after 10 cycles of stripping/plating; (c) XPS spectra and the P 2p, S 2p and F 1s spectrum of Na@NaPS-3 after cycling.

cycling. Meanwhile, the surface of the Na foil becomes very rough and porous with the formation of dead Na. These types of mossy/dendritic Na will further lead to the formation of dead sodium during the plating/stripping process, which will decrease the CE and consume active Na as well as the electrolyte. More SEM images of Na foil after cycling are shown in Fig. S12.† Large moss-like and porous dead Na particles are observed from different areas on the Na foil. Promisingly, with the NaPS coating layers, the surface morphology of Na after electrochemical plating/stripping is relativity smooth and does not possess any high surface area porous structures, as shown in Fig. 3(b). The flake-like coating layers can be clearly seen on the surface of Na@NaPS-3, indicating that the NaPS protective layers remain after cycling. Fig. S12(e–g)† displays similar SEM images of Na@NaPS-3 after cycling from another area of the electrode demonstrating the relatively uniform and smooth surface enabled by the NaPS protection layers.

XPS testing was performed to determine the surface chemical nature of Na foil and the Na@NaPS-3 electrode after electrochemical plating and stripping. The full XPS spectra and high resolution XPS spectrum of P 2p, S 2p and F 1s of Na@NaPS-3 after cycling are shown in Fig. 4(c). From the full XPS spectra, both S 2p and P 2p peaks arising from the NaPS film can be observed after cycling. In the F 1s spectrum, the peak at 686 eV is due to residual Na_xPF_y and $Na_xPO_yF_z$ generated from the electrolyte on the surface, which is consistent with the peaks at 137 eV for the P 2p spectrum. It is apparent that both the S 2p and P 2p peaks are similar to that of the spectrum from the original Na@NaPS-3 samples shown in Fig. 1, which are attributed to the characteristic signal of PS_4^{3-} in the Na_3PS_4 films. The XPS results show that the NaPS protective layers are very robust and can retain their structure after electrochemical cycling.

Furthermore, TOF-SIMS was employed to study the surface and elemental depth distributions of Na@NaPS-3 after cycling. Fig. S14† shows the ion images of Na^-, P^-, S^- and S_2^- of Na@NaPS-3 after electrochemical cycling (images before and after depth profile sputtering). From the ion images before depth profile sputtering, signals arising from P^- and S^- species are seen to be distributed uniformly on the surface. After sputtering by Cs^+ ions, different negative ions of P^-, S^-, and S_2^- show stronger signals from the edge of the sputtering areas, indicating that the NaPS film is electrochemically stable and remains intact. Fig. 4(e) shows the depth profiles of F^-, Na^-, P^-, S^-, S_2^- and PF_6^- for Na@NaPS-3 after cycling. Combined with the ion images in Fig. S15† of F^- and PF_6^-, the top surface of the Na@NaPS-3 after cycling is covered with the salt of $NaPF_6$, which is also consistent with XPS results. After sputtering, the $NaPF_6$ is almost completely removed and the signals of other species of P^-, S^- and S_2^- significantly increase. After 350 s, the concentration of P^-, S^-, and S_2^- ions from the NaPS film decreases, indicating that the thickness of the NaPS film shows a very small change after cycling when compared with the profiles shown in Fig. 2(c).

In conclusion, we first demonstrate a facile and *in situ* solution-based method to fabricate a solid-state electrolyte Na_3PS_4 protective layer on the Na metal anode for long life Na metal batteries. The thickness and chemical composition of the NaPS layers can be controlled by adjusting the precursor concentrations and reaction times, and have been optimized in our study. By protecting the Na foil with Na_3PS_4, the mossy and dendrite-like Na growth is effectively suppressed. From the symmetric cell testing, Na@NaPS-3 displays the most stable electrochemical performances with lower polarization compared with Na foil. Meanwhile, the optimized Na@NaPS-3 can achieve much better performances with large capacities and current densities required for practical applications. It is believed that our design of the Na_3PS_4-coated Na anode can open up new opportunities for the realization of next-generation high energy density Na metal batteries.

Conflicts of interest

There are no conflicts to declare.

Acknowledgements

X. Sun conceived the overall project. Y. Zhao, J. Liang and Q. Sun designed the experiments. Y. Z. performed and completed

the experiments and data analysis and wrote the manuscript. L. Goncharova helped in the RBS testing and analysis. J. Wang and C. Wang carried out the full cell testing. F. Zhao and Y. Sun performed the physical characterization techniques. K. Adair, X. Li and R. Li interpreted the results and data analysis. All authors read and commented on the manuscript. This research was supported by the Natural Science and Engineering Research Council of Canada (NSERC), the Canada Research Chair Program (CRC), the Canada Foundation for Innovation (CFI), and the University of Western Ontario (UWO). We gratefully acknowledge Dr Heng-Yong Nie for his help in the discussion on TOF-SIMS results. We would like to acknowledge the technical expertise of Mr Jack Hendriks at the Western Tandetron accelerator facility.

References

1 J. Y. Hwang, S. T. Myung and Y. K. Sun, *Chem. Soc. Rev.*, 2017, **46**(12), 3529–3614.
2 H. Yadegari, M. Norouzi Banis, A. Lushington, Q. Sun, R. Li, T.-K. Sham and X. Sun, *Energy Environ. Sci.*, 2017, **10**(1), 286–295.
3 H. Yadegari, Y. Li, M. N. Banis, X. Li, B. Wang, Q. Sun, R. Li, T.-K. Sham, X. Cui and X. Sun, *Energy Environ. Sci.*, 2014, **7**(11), 3747–3757.
4 X. B. Cheng, R. Zhang, C. Z. Zhao and Q. Zhang, *Chem. Rev.*, 2017, **117**(15), 10403–10473.
5 S. Wei, S. Choudhury, Z. Tu, K. Zhang and L. A. Archer, *Acc. Chem. Res.*, 2018, **51**(1), 80–88.
6 W. Luo and L. Hu, *ACS Cent. Sci.*, 2015, **1**(8), 420–422.
7 D. Lin, Y. Liu and Y. Cui, *Nat. Nanotechnol.*, 2017, **12**(3), 194–206.
8 R. Zhang, N. W. Li, X. B. Cheng, Y. X. Yin, Q. Zhang and Y. G. Guo, *Adv. Sci.*, 2017, **4**(3), 1600445.
9 Y. Zhao, L. V. Goncharova, Q. Sun, X. Li, A. Lushington, B. Wang, R. Li, F. Dai, M. Cai and X. Sun, *Small Methods*, 2018, 1700417.
10 Z. W. Seh, J. Sun, Y. Sun and Y. Cui, *ACS Cent. Sci.*, 2015, **1**(8), 449–455.
11 J. Zheng, S. Chen, W. Zhao, J. Song, M. H. Engelhard and J.-G. Zhang, *ACS Energy Lett.*, 2018, **3**(2), 315–321.
12 D. Ruiz-Martínez, A. Kovacs and R. Gómez, *Energy Environ. Sci.*, 2017, **10**(9), 1936–1941.
13 S. Wei, S. Choudhury, J. Xu, P. Nath, Z. Tu and L. A. Archer, *Adv. Mater.*, 2017, **29**(12), 1605512.
14 Y. J. Kim, H. Lee, H. Noh, J. Lee, S. Kim, M. H. Ryou, Y. M. Lee and H. T. Kim, *ACS Appl. Mater. Interfaces*, 2017, **9**(7), 6000–6006.
15 W. Luo, Y. Zhang, S. Xu, J. Dai, E. Hitz, Y. Li, C. Yang, C. Chen, B. Liu and L. Hu, *Nano Lett.*, 2017, **17**(6), 3792–3797.
16 A. P. Cohn, N. Muralidharan, R. Carter, K. Share and C. L. Pint, *Nano Lett.*, 2017, **17**(2), 1296–1301.
17 S. Liu, S. Tang, X. Zhang, A. Wang, Q. H. Yang and J. Luo, *Nano Lett.*, 2017, **17**(9), 5862–5868.
18 Y. Lu, Q. Zhang, M. Han and J. Chen, *Chem. Commun.*, 2017, **53**(96), 12910–12913.
19 Y. Xu, A. S. Menon, P. P. R. M. L. Harks, D. C. Hermes, L. A. Haverkate, S. Unnikrishnan and F. M. Mulder, *Energy Storage Materials*, 2018, **12**, 69–78.
20 Y. Zhao, X. Yang, L. Y. Kuo, P. Kaghazchi, Q. Sun, J. Liang, B. Wang, A. Lushington, R. Li, H. Zhang and X. Sun, *Small*, 2018, **14**(20), 1703717.
21 Y. Zhao, K. R. Adair and X. Sun, *Energy Environ. Sci.*, 2018, **11**, 2673–2695.
22 R. Dugas, A. Ponrouch, G. Gachot, R. David, M. R. Palacin and J. M. Tarascon, *J. Electrochem. Soc.*, 2016, **163**(10), A2333–A2339.
23 J. Lee, Y. Lee, J. Lee, S. M. Lee, J. H. Choi, H. Kim, M. S. Kwon, K. Kang, K. T. Lee and N. S. Choi, *ACS Appl. Mater. Interfaces*, 2017, **9**(4), 3723–3732.
24 S. Choudhury, S. Wei, Y. Ozhabes, D. Gunceler, M. J. Zachman, Z. Tu, J. H. Shin, P. Nath, A. Agrawal, L. F. Kourkoutis, T. A. Arias and L. A. Archer, *Nat. Commun.*, 2017, **8**(1), 898.
25 W. Luo, C.-F. Lin, O. Zhao, M. Noked, Y. Zhang, G. W. Rubloff and L. Hu, *Adv. Energy Mater.*, 2017, **7**(2), 1601526.
26 H. Wang, C. Wang, E. Matios and W. Li, *Nano Lett.*, 2017, **17**(11), 6808–6815.
27 Y. Zhao, L. V. Goncharova, A. Lushington, Q. Sun, H. Yadegari, B. Wang, W. Xiao, R. Li and X. Sun, *Adv. Mater.*, 2017, **29**(18), 1606663.
28 Y. Zhao, L. V. Goncharova, Q. Zhang, P. Kaghazchi, Q. Sun, A. Lushington, B. Wang, R. Li and X. Sun, *Nano Lett.*, 2017, **17**(9), 5653–5659.
29 Q. Pang, X. Liang, A. Shyamsunder and L. F. Nazar, *Joule*, 2017, **1**(4), 871–886.
30 Y. Lu, S. Gu, X. Hong, K. Rui, X. Huang, J. Jin, C. Chen, J. Yang and Z. Wen, *Energy Storage Materials*, 2018, **11**, 16–23.
31 S. Wenzel, D. A. Weber, T. Leichtweiss, M. R. Busche, J. Sann and J. Janek, *Solid State Ionics*, 2016, **286**, 24–33.
32 C. Wang, H. Wang, E. Matios, X. Hu and W. Li, *Adv. Funct. Mater.*, 2018, **28**, 1802282.
33 H. Wang, C. Wang, E. Matios and W. Li, *Angew. Chem., Int. Ed.*, 2018, **57**, 7734.